Axial–Equatorial Halide Ordering in Layered Hybrid Perovskites from Isotropic–Anisotropic ^{207}Pb NMR

How to cite: *Angew. Chem. Int. Ed.* **2024**, *63*, e202314856
doi.org/10.1002/anie.202314856

NMR Spectroscopy

Axial–Equatorial Halide Ordering in Layered Hybrid Perovskites from Isotropic–Anisotropic ^{207}Pb NMR

*Michael A. Hope, Manuel Cordova, Aditya Mishra, Ummugulsum Gunes, Alessandro Caiazzo, Kunal Datta, René A. J. Janssen, and Lyndon Emsley**

Abstract: Bandgap-tuneable mixed-halide 3D perovskites are of interest for multi-junction solar cells, but suffer from photoinduced spatial halide segregation. Mixed-halide 2D perovskites are more resistant to halide segregation and are promising coatings for 3D perovskite solar cells. The properties of mixed-halide compositions depend on the local halide distribution, which is challenging to study at the level of single octahedra. In particular, it has been suggested that there is a preference for occupation of the distinct axial and equatorial halide sites in mixed-halide 2D perovskites. ^{207}Pb NMR can be used to probe the atomic-scale structure of lead-halide materials, but although the isotropic ^{207}Pb shift is sensitive to halide stoichiometry, it cannot distinguish configurational isomers. Here, we use 2D isotropic–anisotropic correlation ^{207}Pb NMR and relativistic DFT calculations to distinguish the [PbX_6] configurations in mixed iodide–bromide 3D $FAPb(Br_{1-x}I_x)_3$ perovskites and 2D $BA_2Pb(Br_{1-x}I_x)_4$ perovskites based on formamidinium (FA^+) and butylammonium (BA^+), respectively. We find that iodide preferentially occupies the axial site in BA-based 2D perovskites, which may explain the suppressed halide mobility.

Introduction

Mixed iodide–bromide lead perovskites are promising wide-bandgap absorbers for tandem solar cells.[1–5] Halide alloying allows the bandgap to be tailored, but photoinduced halide migration results in segregation to iodide-rich and bromide-rich phases.[6–8] Three-dimensional (3D) perovskites are also susceptible to degradation under environmental conditions.[9–11] Two-dimensional (2D) perovskites, where layers of corner-sharing lead-halide octahedra are spaced by layers of bulky organic cations (Figure 1), are significantly more stable than their 3D counterparts.[11–14] As a result, 2D

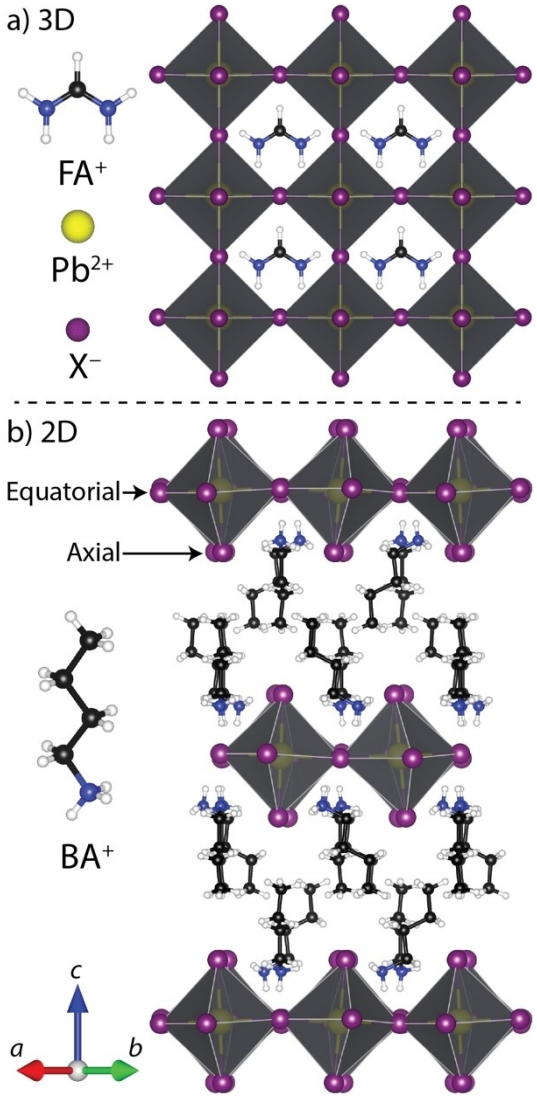

Figure 1. Structures of (a) 3D perovskite $FAPbX_3$ and (b) 2D perovskite BA_2PbX_4, where $X^- = Br^-$ or I^-, FA^+ = formamidinium, and BA^+ = butylammonium. Based on CCDC entries 1584309 and 665690.[45–46]

[*] M. A. Hope, M. Cordova, A. Mishra, U. Gunes, L. Emsley
Institut des Sciences et Ingénierie Chimiques, École Polytechnique Fédérale de Lausanne (EPFL), CH-1015 Lausanne, Switzerland
E-mail: lyndon.emsley@epfl.ch
A. Caiazzo, K. Datta, R. A. J. Janssen
Molecular Materials and Nanosystems, Institute of Complex Molecular Systems, Eindhoven University of Technology, P.O. Box 513, 5600 MB, Eindhoven, The Netherlands

perovskites have shown great promise as coatings on 3D perovskites to maximise both efficiency and stability.[11–13,15–18] Intriguingly, it has been found that mixed-halide 2D perovskites also exhibit suppressed halide mobility and are resistant to photoinduced halide segregation.[19–24]

Unlike 3D perovskites, where all halides are shared between two lead-halide octahedra, there are two types of halide sites in 2D perovskites: equatorial sites that are shared between two octahedra, and axial sites that are only bonded to a single lead atom (Figure 1). The axial halide can also form hydrogen bonds with the organic cation.[25] Consequently, in mixed-halide 2D perovskites, there may be a preference for the different halides to occupy one site or the other. Unlike spatial halide heterogeneity at the nanoscale or microscale, which has been widely studied for 2D and 3D perovskites,[6–8,26–30] halide heterogeneity at the atomic scale of single octahedra is largely unknown. Theoretical calculations of pure 2D (i.e. $n=1$) $PEA_2Pb(Br_{1-x}I_x)_4$ (PEA^+ = phenethylammonium) indicated an enthalpic preference for iodide to occupy the axial sites,[31–32] and single-crystal X-ray diffraction (XRD) data for quasi-2D ($n=2$) $BA_2MAPb_2(Br_{0.5}I_{0.5})_7$ (BA^+ = butylammonium, MA^+ = methylammonium) similarly showed a preference for iodide to occupy the external axial sites[33] (in this case there are two layers of lead halide octahedra per inorganic layer, so there is also an internal axial site that is shared between two octahedra). It has been proposed that the preferential distribution of halide ions is the underlying reason for suppressed halide mobility and enhanced photostability of mixed-halide 2D perovskites.[24,32–33] However, experimental atomic-scale evidence for axial–equatorial halide ordering in pure 2D mixed-halide perovskites is, as yet, lacking.

Solid-state NMR is extremely sensitive to the local arrangement of atoms,[34] making it ideally suited to study halide ordering in 2D perovskites. Furthermore, there is no requirement for large single crystals, which have not been possible to grow for pure-2D mixed-halide perovskites. Solid-state NMR has been successfully applied to address a range of questions for halide perovskite systems,[35–37] and, in particular, ^{207}Pb NMR is sensitive to the halide configuration in mixed iodide–bromide and bromide–chloride 3D perovskites,[38–42] as well as to the number of lead halide layers (n) in quasi-2D $BA_2MA_{n-1}Pb_nI_{3n+1}$ and $PEA_2FA_{n-1}Pb_nI_{3n+1}$ perovskites (FA^+ = formamidinium).[43–44] We recently investigated the isotropic ^{207}Pb shifts of mixed $PEA_2Pb(Br_{1-x}I_x)_4$ 2D perovskites, which indicated a halide distribution that was not ordered but also not fully random;[24] however, due to overlap of different configurations, a full analysis from the isotropic shifts was not possible.

Chemical shift anisotropy (CSA) can be used to extract additional information about local environments in solid-state NMR, beyond that encoded by the isotropic chemical shift.[34] For 3D perovskites, the isotropic ^{207}Pb shift of a local configuration $[PbBr_{6-a}I_a]$ depends approximately linearly on the number of iodine ions, a; however, the isotropic shifts of different isomers with the same composition are very similar, so they cannot be distinguished.[41] The situation is compounded for 2D perovskites, where the lower symmetry results in many more distinct configurational isomers (Figure S1). The ^{207}Pb CSA, on the other hand, measures the deviation from octahedral symmetry so differs significantly for different isomeric configurations, which could, in principle, be used to distinguish them. Initial explorations into ^{207}Pb CSA in 3D perovskites have been made using 1D experiments as a function of magnetic field and magic-angle spinning (MAS) speed,[40] but this approach is extremely challenging due to broad linewidths and overlapping signals. An alternative means to extract both the isotropic and anisotropic chemical shifts is to use a 2D isotropic–anisotropic correlation experiment, such as PASS (phase-adjusted spinning sidebands).[47]

Extracting atomic-scale structural information from experimental chemical shift data often requires comparison with values computed for model systems.[48–52] For systems containing heavy elements such as ^{207}Pb, relativistic effects must be considered to obtain accurate calculated parameters. This can be achieved by constructing clusters and calculating shifts using the gauge-including atomic orbitals (GIAO) formalism, and the zeroth-order regular approximation (ZORA) to account for relativistic effects at the spin-orbit level.[41,53–56]

Here, we use 2D isotropic–anisotropic ^{207}Pb NMR to determine the halide configurations in mixed bromide–iodide perovskites, by comparison with relativistic density functional theory (DFT) calculations. We start with 3D $FAPb(Br_{1-x}I_x)_3$ perovskites, distinguishing the different $[PbX_6]$ configurations and measuring their ^{207}Pb CSAs. We then investigate 2D $BA_2Pb(Br_{1-x}I_x)_4$ perovskites, providing the first atomic-scale experimental evidence that iodide preferentially occupies the axial sites in pure 2D perovskites.

Results and Discussion

To validate the ^{207}Pb PASS experiment we used δ-$CsPbI_3$, which is a non-perovskite phase with a large CSA. These lead halide systems suffer from fast transverse relaxation, therefore it is beneficial to use a PASS experiment with a single rotor period for evolution; however, it is then challenging to fit the five required π pulses and satisfy the PASS timing equations.[47] We found that this was possible using a 1.3 mm probe with a radiofrequency (rf) power of 250 kHz (2 μs for a π pulse), with a spinning rate of up to 24 kHz (41.7 μs rotor period); the high rf power is also beneficial to excite the full ^{207}Pb spectrum. With these parameters, it was possible to accurately extract the isotropic shift and CSA parameters (Figure S2); the isotropic shift and CSA parameters for δ-$CsPbI_3$ differ from previous reports,[40,42] which is ascribed to insufficient excitation bandwidth and mis-assignment of the centreband.

We then used ^{207}Pb PASS and relativistic DFT calculations to distinguish the Pb configurations in 3D $FAPb(Br_{1-x}I_x)_3$ perovskites. Powdered samples with $x=$ 0, 0.25, 0.5, 0.75 and 1 were prepared by mechanosynthesis, see

the Experimental section in the Supporting Information. Figure 2 shows the isotropic ^{207}Pb spectra obtained by summation of the corresponding PASS spectra. The peaks for pure $FAPbI_3$ and $FAPbBr_3$ occur at 1500 ppm and 520 ppm, respectively, whereas the mixed compositions yield broad overlapping resonances that are intermediate between those of the end-members. There is a trend in the isotropic ^{207}Pb spectra as a function of halide content, but the different configurations cannot be readily distinguished, as previously observed.[38–41]

The anisotropic ^{207}Pb shift provides a means by which to distinguish the lead–halide configurations. Figure 3 shows the full 2D PASS ^{207}Pb spectra for the same samples, which clearly discriminate between the isotropic environments of the pure-halide perovskites, and the anisotropic environments of mixed-halide configurations. To extract the CSA parameters of the different configurations, the spectra for $x = 0.25$, 0.5, and 0.75 were simultaneously fitted using the Mrsimulator python package.[57] In the fitting procedure, the isotropic and anisotropic shifts were refined using the relativistic DFT calculations of $[PbX_6]^{4-}$ clusters by Askar et al.[41] as a starting point, and the intensities of each configuration were calculated from the binomial distribution with an apparent halide composition that was allowed to vary. Full details are given in the Supporting Information.

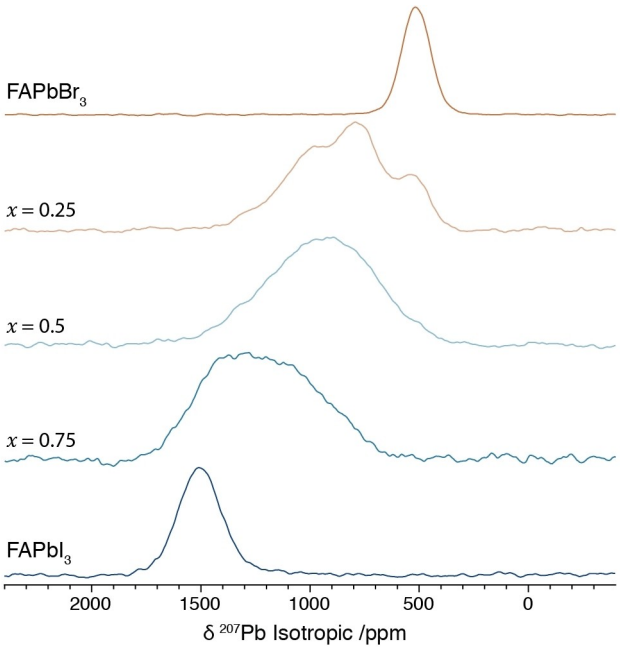

Figure 2. Experimental isotropic ^{207}Pb NMR spectra of 3D $FAPb(Br_{1-x}I_x)_3$ perovskites, obtained from summation of the PASS spectra, at 12.5 kHz MAS and 11.7 T.

Figure 4a shows the fitted 2D PASS spectra, while isotropic and anisotropic 1D summations are shown in Figure S4 and the fitted spectral parameters are given in Table S2. This demonstrates that the fitting procedure can successfully reproduce the experimental data. Figure 4b shows the contribution from each configuration in the fitted PASS spectra, which highlights how the CSA helps to distinguish the configurations. For example, the two isomers of $[PbBr_3I_3]$ have the same isotropic ^{207}Pb shift, but the CSA for the *fac* isomer is near zero, while that of the *mer* isomer is much larger (see Table S2). Figure 5 shows a comparison of the fitted and calculated isotropic and anisotropic shifts. There is a good linear agreement between the calculated isotropic shielding and the fitted experimental isotropic shift (Figure 5a), as was also reported for the more resolved spectra of mixed Br–Cl perovskites.[40] For the CSA (Figure 5b), there is a strong correlation between the fitted and calculated values, lending confidence to both, although the calculations underestimate the CSA on average by ~27 %. There is also greater scatter between the calculated and experimental values, which could arise from errors in both the calculation of ^{207}Pb CSA using relativistic DFT and fitting of the experimental PASS spectrum to extract the experimental CSA. The fitted sample compositions (Table S3) for $x = 0.50$ and 0.75 are significantly lower than the nominal sample compositions; this is ascribed to faster transverse relaxation for iodide-rich configurations compared to bromide-rich configurations (Figure S3). Consequently, the intensities here should be viewed as semi-quantitative, but this is not expected to have a significant effect on the fitted shift parameters. Finally, it should be stressed that the deconvolution of the 2D PASS spectrum is not unique and the agreement between the calculated and

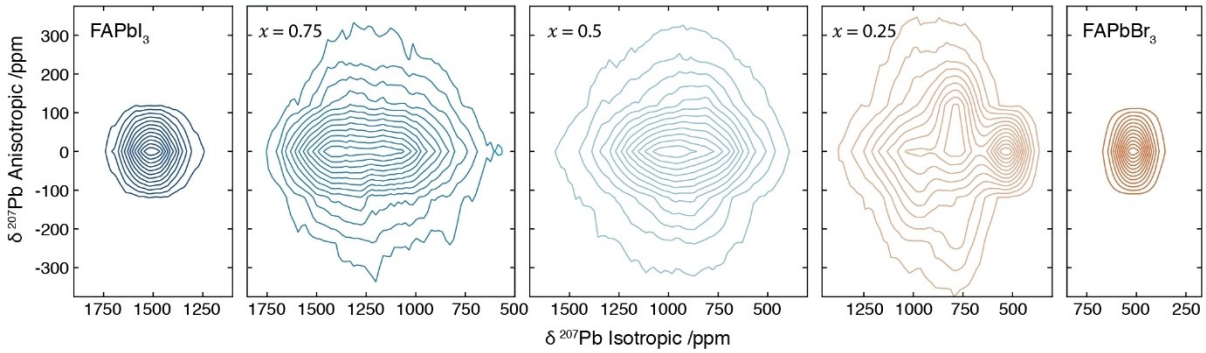

Figure 3. Experimental ^{207}Pb PASS spectra of 3D $FAPb(Br_{1-x}I_x)_3$ perovskites at 12.5 kHz MAS and 11.7 T. The 12 contours are linearly spaced between 8 % and 92 % of the maximum intensity.

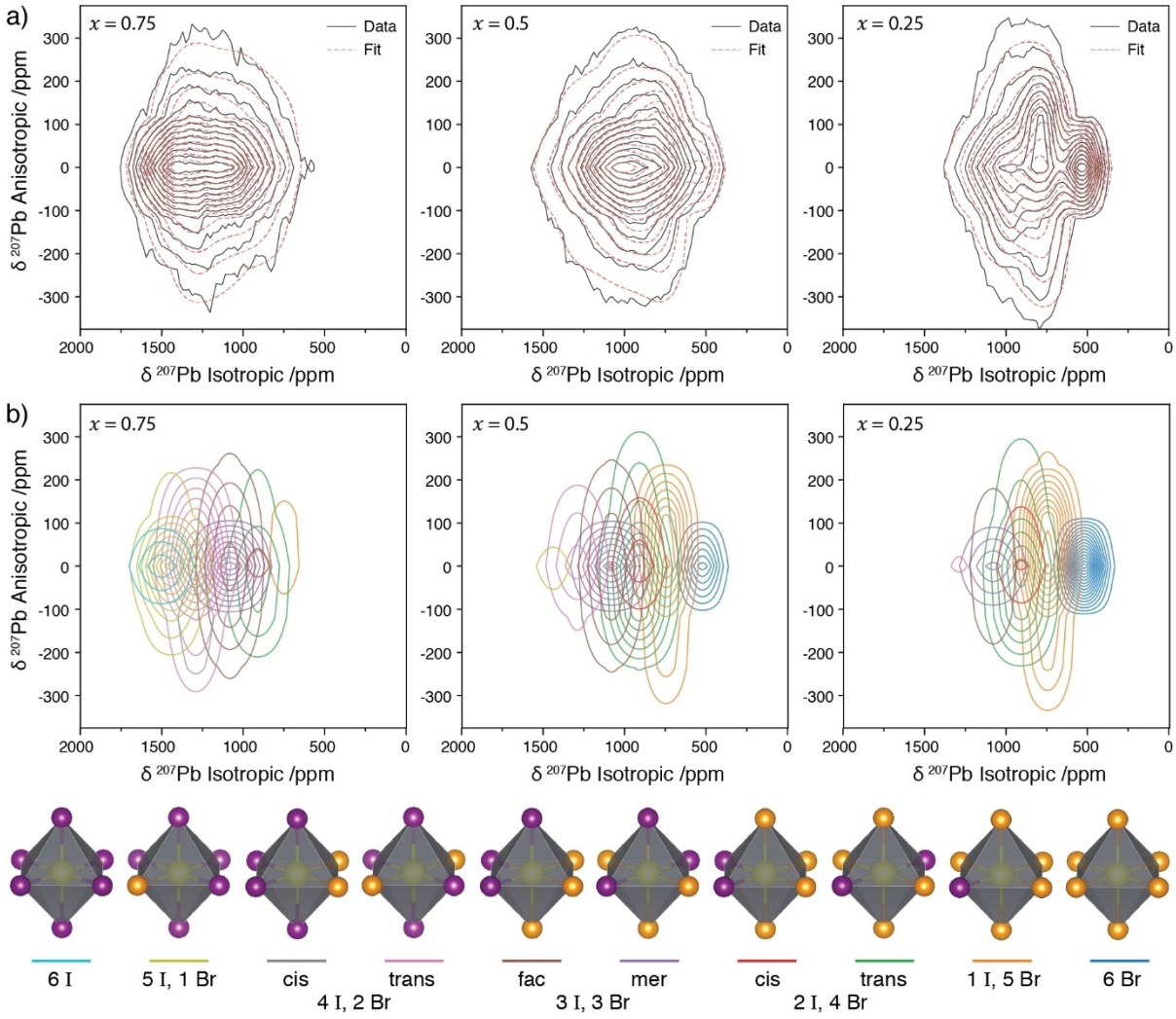

Figure 4. Fitting of the ^{207}Pb PASS spectra of 3D FAPb($Br_{1-x}I_x$)$_3$ perovskites. a) Experimental and fitted spectra. 12 contours are linearly spaced between 8% and 92% of the maximum intensity. b) Deconvolution of the fitted spectra into the component configurations, shown at the bottom. 18 contour levels are linearly spaced between 5% and 95% of the maximum intensity. Purple and gold spheres represent iodide and bromide ions, respectively. Fitting parameters are given in Table S2.

fitted shift parameters is facilitated by starting the fitting procedure from the calculated values. Nevertheless, by combining relativistic DFT calculations of the full shielding tensor with the experimental 2D isotropic–anisotropic correlation spectrum, the different [PbX_6] configurations can be distinguished and their CSAs determined. Notably, this is the first experimental determination of the ^{207}Pb CSA in mixed I–Br perovskites.

Having demonstrated the utility of isotropic–anisotropic ^{207}Pb NMR for 3D perovskites, we now turn to butylammonium-based 2D perovskites, $BA_2Pb(Br_{1-x}I_x)_4$. Unlike pure-halide 3D perovskites, the pure-halide 2D perovskites exhibit non-zero ^{207}Pb CSA due to the anisotropy of the layered structure, which can be seen in both the static and MAS PASS spectra (Figure 6). BA_2PbI_4 and BA_2PbBr_4 exhibit approximately axial CSAs, consistent with the layered structure where the directions in the *ab* plane are similar, but distinct to the out-of-plane *c* direction (Figure 1). The CSAs for both BA_2PbI_4 and BA_2PbBr_4 are negative, indicating that the ^{207}Pb shift is greater in the in-plane directions than out-of-plane, i.e. $\delta_{xx} \approx \delta_{yy} > \delta_{zz}$ (Table 1); this is evidenced by the greater intensity at higher shift/sideband order in both the static and MAS PASS spectra (Figure 6). The CSA is larger for BA_2PbI_4 than for BA_2PbBr_4. The isotropic shift for BA_2PbI_4 (1065 ppm) is in agreement with previous literature (noting that the shift is temperature dependent),[43] and a lower isotropic shift is observed for BA_2PbBr_4 (105 ppm), in line with the trend observed for 3D perovskites. The isotropic ^{207}Pb shifts for both materials are ca. 450 ppm lower than their FA-based 3D counterparts.

The ^{207}Pb PASS spectra of mixed-halide 2D $BA_2Pb(Br_{1-x}I_x)_4$ perovskites are shown in Figure 7. Consistent with the 3D perovskites, the isotropic shifts vary systematically with the halide alloying (see Figure S5 for the isotropic summations), and the CSAs of the mixed composi-

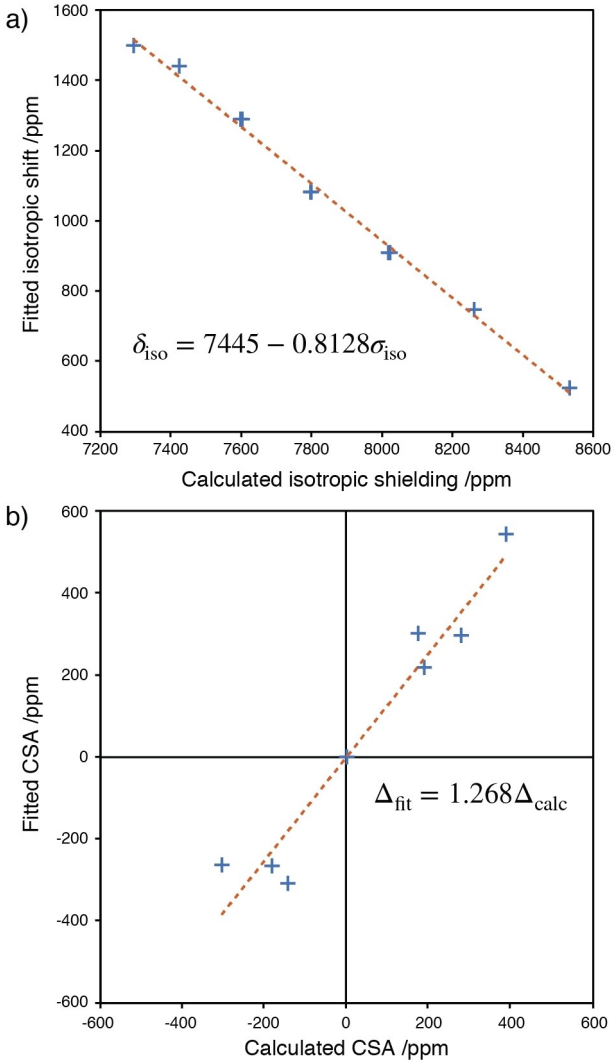

Figure 5. Comparison of fitted and calculated a) isotropic and b) anisotropic ^{207}Pb shifts for the [PbX_6] configurations in 3D $FAPb(Br_{1-x}I_x)_3$ perovskites. Lines of best fit are shown dashed and the corresponding equations are given. The calculated values are taken from Askar et al.[41]

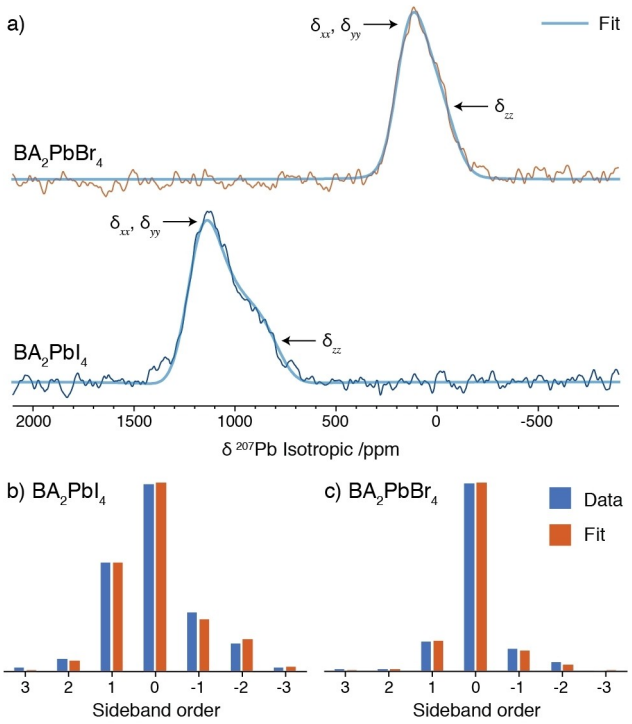

Figure 6. ^{207}Pb NMR of BA_2PbBr_4 and BA_2PbI_4 at 11.7 T. a) Non-spinning spectra with the simulated CSA patterns. b,c) Sideband intensities determined from the 2D PASS spectra at 12.5 kHz MAS and the fitted intensities. Shift parameters are given in Table 1.

Table 1: Experimental shift and calculated shielding parameters for pure-halide BA_2PbBr_4 and BA_2PbI_4.

Experimental			Calculated		
	BA_2PbI_4	BA_2PbBr_4		BA_2PbI_4	BA_2PbBr_4
δ_{iso}/ppm*	1065	105	σ_{iso}/ppm	7133	8304
Δ/ppm	−270	−163	Δ/ppm†	159	180
η	0	0	η	0.05	0.12
δ_{xx}/ppm	1200	187	σ_{xx}/ppm	7216	8404
δ_{yy}/ppm	1200	187	σ_{yy}/ppm	7208	8383
δ_{zz}/ppm	795	−58	σ_{zz}/ppm	6974	8124

*At room temperature and 24 kHz MAS, in a 1.3 mm rotor, without active temperature control.
†The shift anisotropy of the calculated tensor is given to allow direct comparison, rather than the shielding anisotropy which has the opposite sign.

tions are significantly larger than for the end-members, reflecting the anisotropy of mixed-halide configurations. The ^{207}Pb CSAs of mixed-halide 2D perovskite configurations are also larger than for 3D perovskites (the *y* axis scale in Figure 7 is 2.4× larger than that of Figure 3), indicating an additive effect of the anisotropies introduced by the layered structure and halide alloying.

There are 18 possible distinct [$PbBr_{6-a}I_a$] configurations in 2D perovskites (Figure S1); to interpret the ^{207}Pb PASS spectra, we performed relativistic DFT calculations for all these configurations. First, the experimental pure-halide structures and 10 mixed-halide structures constructed by atomic substitution (containing all 18 possible configurations) were relaxed with periodic DFT, allowing all atomic positions to refine (relaxed structures are given in the data repository). $[BA_8Pb_5X_{26}]^{8-}$ clusters were then extracted centred on each Pb atom in the relaxed structures, comprising the central [PbX_6] octahedron, the four adjacent [PbX_6] octahedra, and the eight adjacent BA^+ cations (Figure S6). The shielding of the central ^{207}Pb atom was then calculated for each cluster using the GIAO formalism and ZORA treatment of relativistic effects up to spin–orbit coupling. Full details are given in the Experimental.

The calculated ^{207}Pb shieldings for BA_2PbBr_4 and BA_2PbI_4 are given in Table 1. Both yield an approximately axial CSA tensor (small η) as expected, with the unique *z* axis approximately aligned with the out-of-plane *c* direction of the crystal structure. However, the CSA is calculated to be positive not negative, i.e., the *zz* component is calculated

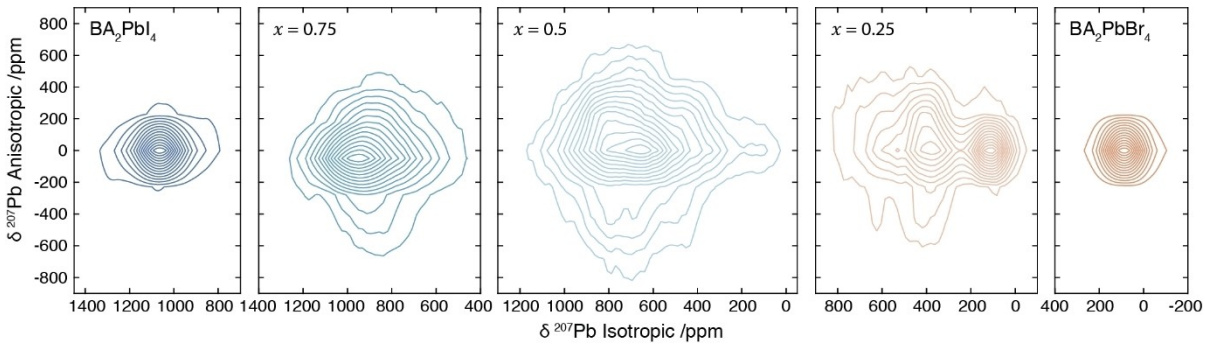

Figure 7. Experimental ^{207}Pb PASS spectra of 2D $BA_2Pb(Br_{1-x}I_x)_4$ perovskites at 24 kHz MAS and 11.7 T. The 14 contour levels are linearly spaced between 7% and 93% of the maximum intensity.

to have the smallest shielding, rather than the largest. This most likely arises from the electronic structure of the perovskite layers not being correctly captured in the calculations, requiring either a higher level of theory or a larger cluster, neither of which are achievable with current methods. We note that Kye et al. ascribe the predominance of negative ^{207}Pb CSA to occupation of the p_z orbital by the Pb lone pair.[58] Nevertheless, in order to calculate the shift parameters for the mixed-halide configurations we need only to interpolate between the pure-bromide and pure-iodide materials, and since the full experimental shift tensors and calculated shielding tensors are known for the end-members, we can account for the layered structure by using different shift–shielding regressions for the in plane and out-of-plane directions (see the experimental section for details). The respective regressions are given in Table S1. Using these regressions, the shift tensor was calculated from the shielding tensor for each mixed-halide cluster (Table S4). As was the case for 3D perovskites, the isotropic ^{207}Pb shift depends primarily on the halide stoichiometry (Figure S7), while the ^{207}Pb CSA is highly sensitive to the configuration.

With the calculated ^{207}Pb tensors for all the 2D perovskite $[PbX_6]$ configurations, we now fit the experimental ^{207}Pb PASS spectra. To better constrain the ^{207}Pb CSA, the ^{207}Pb PASS spectra for $x = 0.25$, 0.5, and 0.75 samples were recorded at both 18 kHz MAS and 24 kHz MAS. All six spectra were then simultaneously fitted using Mrsimulator. The isotropic shift for each configuration was fixed to the calculated value and the CSA was allowed to vary from the calculated value with a single global scaling factor for all configurations.

To account for preferential halide occupation of the axial/equatorial sites, we introduce an axial–equatorial ordering parameter, $-1 < k < +1$, such that the probability that an axial/equatorial site is occupied by iodide (p_{ax}, p_{eq}) is given by:

$$x < 0.5 \;:\; p_{ax} = (1+k)x, \qquad p_{eq} = (1-k)x \tag{1}$$

$$x > 0.5 \;:\; p_{ax} = (1-k)x + k, \quad p_{eq} = (1+k)x - k, \tag{2}$$

where x is the iodide composition. Here, positive k corresponds to preference for iodide to occupy the axial site and negative k for iodide to occupy the equatorial site; see Figure S8 for further discussion and Figure S9 for a schematic illustration. The probability of a configuration with n_{ax} axial iodides and n_{eq} equatorial iodides is then:

$$p(n_{ax}, n_{eq}) = d\left[p_{ax}^{n_{ax}}(1-p_{ax})^{(2-n_{ax})}p_{eq}^{n_{eq}}(1-p_{eq})^{(4-n_{eq})}\right], \tag{3}$$

where d is the degeneracy of that configuration (see Table S4, and Supplementary Note 2 for a derivation). The composition, x, was optimised for each sample and the global order parameter, k, was either fixed to zero or optimised.

The fitted 2D spectra are shown in Figure S11 and the 1D isotropic and anisotropic summations are summarised in Figure 8. The key parameters and reduced chi-squared statistic (χ^2_ν) are given in Table 2, with further parameters in Table S5, Table S6, and Table S7. When the axial–equatorial ordering parameter is allowed to refine, the optimum value is $k = +0.54$, indicating a preference for iodide to occupy

Table 2: Fitted axial–equatorial order parameter, k, fitted CSA scaling factor, and reduced chi-squared (χ^2_ν) for the simulated ^{207}Pb PASS spectra of $BA_2Pb(Br_{1-x}I_x)_4$, with and without allowing the composition and CSA scaling factor to refine.

	Refined Composition				Fixed Composition			
	Vary CSA scale		Fix CSA scale = 1		Vary CSA scale		Fix CSA scale = 1	
	Fix k	Vary k	Fix k	Vary k	Fix k	Vary k	Fix k	Vary k
k	0	0.54	0	0.84	0	0.35	0	0.54
CSA scale	1.82	1.34	1	1	1.84	1.45	1	1
χ^2_ν	12.7	7.7	28.6	10.6	17.4	9.96	33.2	16.7

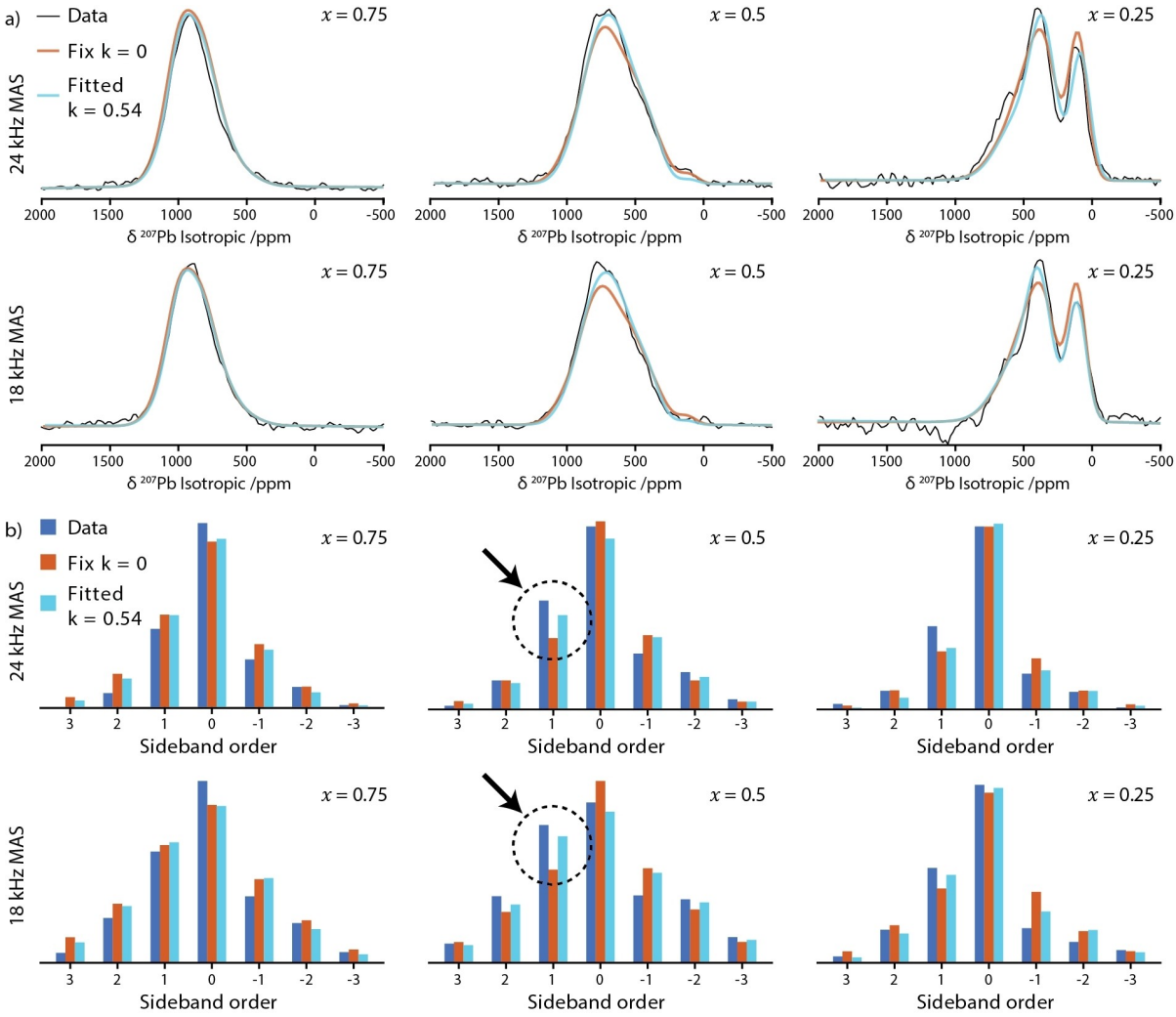

Figure 8. a) Isotropic and b) anisotropic sums of the experimental and fitted ^{207}Pb PASS spectra of 2D $BA_2Pb(Br_{1-x}I_x)_4$ perovskites, at 24 and 18 kHz MAS, with and without allowing k to refine. In both cases the CSA scaling factor was refined. 2D data is shown in Figure S11 and the shift parameters are given in Table S4. The improvement from refining k can most clearly be seen from the +1 order sideband for the $x = 0.5$ sample, which has been highlighted with arrows.

the axial sites. This results in a marked improvement of the fits (Figure 8), with a reduction in χ^2_ν from 12.7 to 7.7 (see the Experimental section for the procedure to calculate χ^2_ν). Furthermore, the optimal CSA scaling factor is reduced from 1.82 to 1.34 when k is refined, which is then comparable to the scaling factor of ~1.27 required above for the 3D $FAPb(Br_{1-x}I_x)_3$ perovskites (Figure 5b).

Configurations with more axial iodides and equatorial bromides have larger, more negative CSAs, and are promoted by the positive k (see Figure S10, Table S4, and Supplementary Note 1). This improves the match between the simulated and experimental PASS spectra, most notably for the +1 order sideband, which is severely underestimated when $k = 0$ (Figure 8b). Halide ordering has the greatest effect on the configurations present for the $x = 0.5$ sample, because it could range from fully ordered $\left[PbI_2^{ax}Br_4^{eq}\right]$ to fully ordered $\left[PbI_2^{eq}Br_4^{ax}\right]$. Note that the equatorial sites are shared between two octahedra so contribute half as much to the sample composition as the axial sites; both of these fully ordered arrangements therefore have a composition of $x = 0.5$.

If the CSA is not allowed to scale there is an even greater improvement in the fit by including a preference for axial iodide (Figure S12, Figure S13, and Table 2), with a reduction in χ^2_ν from 28.6 to 10.6. In fact, varying k alone improves the fit more than scaling the CSA. In this case, the optimal k is +0.84. Similar results are obtained if the composition of each sample is fixed to the nominal value, with optimised ordering parameters of $k = +0.35$ and +0.54 with and without scaling of the CSA, respectively (Table 2, Figures S14–S17).

Ordering parameters of $k = 0.35$, 0.54, and 0.84 correspond to 2.1×, 3.3×, and 11.5× greater probabilities of iodide occupying the axial site than the equatorial (for $x \leq 0.5$; at higher compositions, occupation of the axial site with iodide begins to saturate). This is shown schematically in Figure 9 for $x = 0.5$. The halide distribution is still partially disordered over both the axial and equatorial sites, because

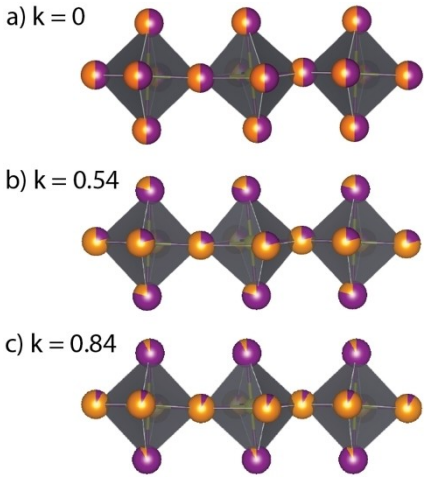

Figure 9. Schematic representation of the axial–equatorial ordering in a 2D mixed-halide $BA_2Pb(Br_{1-x}I_x)_4$ perovskites with $x = 0.5$ and different values of the ordering parameter, *k*. Purple and gold spheres represent iodide and bromide ions and the fractional colouring indicates their respective probability.

$k < 1$, reflecting a balance between the lower enthalpy of iodide occupying the axial site and the greater entropy of disorder. This is most obvious for the $x = 0.5$ sample, where perfect ordering would give only a single peak from the [$PbI_2^{ax}Br_4^{eq}$] configuration, rather than the multiple broad overlapping resonances observed. Due to the difficulty of accurately calculating ^{207}Pb shielding parameters and fitting the 18 overlapping signals in the ^{207}Pb PASS spectra, the results here should be considered as semi-quantitative. There is a clear preference for iodide to occupy the axial site, and we expect the experimental degree of ordering to lie in the range determined here, however there is still significant uncertainty in the exact value. The preference for axial iodide explains the non-linear dependence of the out-of-plane *c* lattice parameter on the halide stoichiometry, as observed here (Table S11) and previously by Toso et al.[33]

We propose that the preference for iodide to occupy the axial sites is the cause of the resistance to spatial halide segregation in mixed iodide–bromide 2D perovskites. A phase segregated mixture of iodide-rich ($x > 0.5$) and bromide-rich ($x < 0.5$) phases has a lower overall probability of iodide occupying the axial site than a mixed phase with the corresponding average composition. Consequently, there is an enthalpic penalty to forming such spatially halide-segregated phases (in addition to the intrinsic entropic disadvantage). Furthermore, preference for axial iodide suppresses the halide mobility because for iodide ions in the axial sites to diffuse, they first move into an equatorial site, again with an energetic penalty.

Finally, we extended our analysis to phenylethylammonium (PEA^+)-based 2D perovskites, since PEA^+ is one of the most commonly used spacer molecules.[12–13] Figure S18 shows the 2D PASS spectra for PEA_2PbI_4 and PEA_2PbBr_4, and the fitted CSA parameters are given in Table S12. We previously used these PASS spectra to extract the isotropic ^{207}Pb spectra of the two samples.[24] Surprisingly, pure-bromide PEA_2PbBr_4 exhibits a large CSA of −450 ppm, significantly higher than for PEA_2PbI_4, BA_2PbI_4, or BA_2PbBr_4. This is ascribed to off-centring of the Pb^{2+} ions within the bromide octahedra, as identified in the experimental crystal structure[59] (Figure S19), resulting in a more anisotropic environment. This off-centring is not present in PEA_2PbI_4 or the BA-based 2D perovskites,[25,45,60] demonstrating that the ^{207}Pb CSA is a sensitive reporter of this phenomenon. Further work determining whether Pb^{2+} off-centring is present in PEA-based mixed-halide materials is required to understand their role as coatings for mixed-halide 3D perovskites. The differing structures of the end-members makes analysis of the ^{207}Pb CSAs for mixed-halide $PEA_2Pb(Br_{1-x}I_x)_4$ more challenging. Nevertheless, it is likely that the preference for axial iodide identified here for BA-based 2D perovskites is also present in PEA-based 2D perovskites, as predicted computationally.[32]

Conclusions

We have shown that the anisotropic ^{207}Pb chemical shift can be used to analyse mixed-halide [PbX_6] configurations in 2D and 3D perovskites by combining 2D PASS NMR, relativistic DFT calculations, and spectral fitting. With this method, we show that iodide preferentially occupies the axial site in mixed iodide–bromide 2D $BA_2Pb(Br_{1-x}I_x)_4$ perovskites. The preference for axial iodide in the sample results in a greater proportion of configurations with larger, negative ^{207}Pb CSAs, which can be clearly seen in the experimental ^{207}Pb PASS spectra. Although our analysis is not fully quantitative, we determine axial–equatorial ordering parameters in the range $k = 0.35$–0.84, which corresponds to between 2× and 12× greater probability of iodide occupying the axial site than the equatorial site. This provides a possible atomic-level basis for the previously observed suppressed halide mobility and enhanced photostability of mixed-halide 2D perovskites.

Acknowledgements

This work was supported by SNSF grant number 200020_212046. M.A.H. acknowledges a H2020 Marie Skłodowska-Curie Individual fellowship with grant number 101024144. We would like to thank Prof. Grandinetti, Dr. Srivastava, and Mr. Giammar (Ohio State University) for support and advice in using Mrsimulator. Open Access funding provided by École Polytechnique Fédérale de Lausanne.

Conflict of Interest

The authors declare no conflict of interest.

Data Availability Statement

Raw and processed NMR and XRD data, DFT calculations, and the python notebooks used for fitting are available at DOI: 10.5281/zenodo.8324046 with a CC-BY-4.0 (Creative Commons Attribution-ShareAlike 4.0 International) license.

Keywords: Ab initio calculations · 2D halide perovskites · Halide segregation · NMR spectroscopy · photovoltaic materials

[1] N. N. Lal, Y. Dkhissi, W. Li, Q. Hou, Y.-B. Cheng, U. Bach, *Adv. Energy Mater.* **2017**, *7*, 1602761.
[2] G. E. Eperon, M. T. Hörantner, H. J. Snaith, *Nat. Chem. Rev.* **2017**, *1*, 0095.
[3] T. Leijtens, K. A. Bush, R. Prasanna, M. D. McGehee, *Nat. Energy* **2018**, *3*, 828–838.
[4] R. Wang, T. Huang, J. Xue, J. Tong, K. Zhu, Y. Yang, *Nat. Photonics* **2021**, *15*, 411–425.
[5] R. Lin, J. Xu, M. Wei, Y. Wang, Z. Qin, Z. Liu, J. Wu, K. Xiao, B. Chen, S. M. Park, G. Chen, H. R. Atapattu, K. R. Graham, J. Xu, J. Zhu, L. Li, C. Zhang, E. H. Sargent, H. Tan, *Nature* **2022**, *603*, 73–78.
[6] E. T. Hoke, D. J. Slotcavage, E. R. Dohner, A. R. Bowring, H. I. Karunadasa, M. D. McGehee, *Chem. Sci.* **2015**, *6*, 613–617.
[7] M. C. Brennan, A. Ruth, P. V. Kamat, M. Kuno, *Trends Chem.* **2020**, *2*, 282–301.
[8] A. J. Knight, L. M. Herz, *Energy Environ. Sci.* **2020**, *13*, 2024–2046.
[9] S. D. Stranks, H. J. Snaith, *Nat. Nanotechnol.* **2015**, *10*, 391–402.
[10] D. Wang, M. Wright, N. K. Elumalai, A. Uddin, *Sol. Energy Mater. Sol. Cells* **2016**, *147*, 255–275.
[11] C. C. Boyd, R. Cheacharoen, T. Leijtens, M. D. McGehee, *Chem. Rev.* **2018**, *119*, 3418–3451.
[12] X. Li, J. M. Hoffman, M. G. Kanatzidis, *Chem. Rev.* **2021**, *121*, 2230–2291.
[13] G. Grancini, M. K. Nazeeruddin, *Nat. Rev. Mater.* **2018**, *4*, 4–22.
[14] H. Tsai, W. Nie, J.-C. Blancon, C. C. Stoumpos, R. Asadpour, B. Harutyunyan, A. J. Neukirch, R. Verduzco, J. J. Crochet, S. Tretiak, L. Pedesseau, J. Even, M. A. Alam, G. Gupta, J. Lou, P. M. Ajayan, M. J. Bedzyk, M. G. Kanatzidis, A. D. Mohite, *Nature* **2016**, *536*, 312–316.
[15] G. Grancini, C. Roldán-Carmona, I. Zimmermann, E. Mosconi, X. Lee, D. Martineau, S. Narbey, F. Oswald, F. De Angelis, M. Graetzel, M. K. Nazeeruddin, *Nat. Commun.* **2017**, *8*, 15684.
[16] Z. Wang, Q. Lin, F. P. Chmiel, N. Sakai, L. M. Herz, H. J. Snaith, *Nat. Energy* **2017**, *2*, 17135.
[17] P. Chen, Y. Bai, S. Wang, M. Lyu, J. H. Yun, L. Wang, *Adv. Funct. Mater.* **2018**, *28*, 1706923.
[18] Y. Liu, S. Akin, A. Hinderhofer, F. T. Eickemeyer, H. Zhu, J. Y. Seo, J. Zhang, F. Schreiber, H. Zhang, S. M. Zakeeruddin, A. Hagfeldt, M. I. Dar, M. Grätzel, *Angew. Chem. Int. Ed.* **2020**, *59*, 15688–15694.
[19] Y. Lin, Y. Bai, Y. Fang, Q. Wang, Y. Deng, J. Huang, *ACS Energy Lett.* **2017**, *2*, 1571–1572.
[20] X. Xiao, J. Dai, Y. Fang, J. Zhao, X. Zheng, S. Tang, P. N. Rudd, X. C. Zeng, J. Huang, *ACS Energy Lett.* **2018**, *3*, 684–688.
[21] J. Cho, J. T. DuBose, A. N. T. Le, P. V. Kamat, *ACS Materials Lett.* **2020**, *2*, 565–570.
[22] P. S. Mathew, J. T. DuBose, J. Cho, P. V. Kamat, *ACS Energy Lett.* **2021**, *6*, 2499–2501.
[23] J. Cho, P. S. Mathew, J. T. DuBose, P. V. Kamat, *Adv. Mater.* **2021**, *33*, 2105585.
[24] K. Datta, A. Caiazzo, M. A. Hope, J. Li, A. Mishra, M. Cordova, Z. Chen, L. Emsley, M. M. Wienk, R. A. J. Janssen, *ACS Energy Lett.* **2023**, *8*, 1662–1670.
[25] K.-z. Du, Q. Tu, X. Zhang, Q. Han, J. Liu, S. Zauscher, D. B. Mitzi, *Inorg. Chem.* **2017**, *56*, 9291–9302.
[26] C. R. Roy, Y. Zhou, D. D. Kohler, Z. Zhu, J. C. Wright, S. Jin, *ACS Energy Lett.* **2022**, *7*, 3423–3431.
[27] A. Zanetta, Z. Andaji-Garmaroudi, V. Pirota, G. Pica, F. U. Kosasih, L. Gouda, K. Frohna, C. Ducati, F. Doria, S. D. Stranks, G. Grancini, *Adv. Mater.* **2021**, *34*, 2105942.
[28] K. Frohna, M. Anaya, S. Macpherson, J. Sung, T. A. S. Doherty, Y.-H. Chiang, A. J. Winchester, K. W. P. Orr, J. E. Parker, P. D. Quinn, K. M. Dani, A. Rao, S. D. Stranks, *Nat. Nanotechnol.* **2021**, *17*, 190–196.
[29] P. Gratia, G. Grancini, J.-N. Audinot, X. Jeanbourquin, E. Mosconi, I. Zimmermann, D. Dowsett, Y. Lee, M. Grätzel, F. De Angelis, K. Sivula, T. Wirtz, M. K. Nazeeruddin, *J. Am. Chem. Soc.* **2016**, *138*, 15821–15824.
[30] J.-P. Correa-Baena, Y. Luo, T. M. Brenner, J. Snaider, S. Sun, X. Li, M. A. Jensen, N. T. P. Hartono, L. Nienhaus, S. Wieghold, J. R. Poindexter, S. Wang, Y. S. Meng, T. Wang, B. Lai, M. V. Holt, Z. Cai, M. G. Bawendi, L. Huang, T. Buonassisi, D. P. Fenning, *Science* **2019**, *363*, 627–631.
[31] N. E. Wright, X. Qin, J. Xu, L. L. Kelly, S. P. Harvey, M. F. Toney, V. Blum, A. D. Stiff-Roberts, *Chem. Mater.* **2022**, *34*, 3109–3122.
[32] Z. Chen, H. Xue, G. Brocks, P. A. Bobbert, S. Tao, *ACS Energy Lett.* **2023**, *8*, 943–949.
[33] S. Toso, I. Gushchina, A. G. Oliver, L. Manna, M. Kuno, *ACS Energy Lett.* **2022**, *7*, 4242–4247.
[34] B. Reif, S. E. Ashbrook, L. Emsley, M. Hong, *Nat. Rev. Methods Primers* **2021**, *1*, 2.
[35] W. M. J. Franssen, A. P. M. Kentgens, *Solid State Nucl. Magn. Reson.* **2019**, *100*, 36–44.
[36] L. Piveteau, V. Morad, M. V. Kovalenko, *J. Am. Chem. Soc.* **2020**, *142*, 19413–19437.
[37] D. J. Kubicki, S. D. Stranks, C. P. Grey, L. Emsley, *Nat. Chem. Rev.* **2021**, *5*, 624–645.
[38] B. A. Rosales, L. Men, S. D. Cady, M. P. Hanrahan, A. J. Rossini, J. Vela, *Chem. Mater.* **2016**, *28*, 6848–6859.
[39] C. Roiland, G. Trippé-Allard, K. Jemli, B. Alonso, J.-C. Ameline, R. Gautier, T. Bataille, L. Le Pollès, E. Deleporte, J. Even, C. Katan, *Phys. Chem. Chem. Phys.* **2016**, *18*, 27133–27142.
[40] A. Karmakar, A. M. Askar, G. M. Bernard, V. V. Terskikh, M. Ha, S. Patel, K. Shankar, V. K. Michaelis, *Chem. Mater.* **2018**, *30*, 2309–2321.
[41] A. M. Askar, A. Karmakar, G. M. Bernard, M. Ha, V. V. Terskikh, B. D. Wiltshire, S. Patel, J. Fleet, K. Shankar, V. K. Michaelis, *J. Phys. Chem. Lett.* **2018**, *9*, 2671–2677.
[42] M. Aebli, L. Piveteau, O. Nazarenko, B. M. Benin, F. Krieg, R. Verel, M. V. Kovalenko, *Sci. Rep.* **2020**, *10*, 8229.
[43] J. Lee, W. Lee, K. Kang, T. Lee, S. K. Lee, *Chem. Mater.* **2020**, *33*, 370–377.
[44] L. Hong, Z. Wang, J. V. Milić, C. E. Avalos, W. Zhang, D. Ren, C. Wang, B. Carlsen, Y. Liu, S. M. Zakeeruddin, A. Hagfeldt, T. Wang, H. Han, M. Graetzel, *Chem. Mater.* **2022**, *34*, 6331–6338.
[45] D. G. Billing, A. Lemmerer, *Acta Crystallogr. Sect. B* **2007**, *63*, 735–747.
[46] C. Zheng, O. Rubel, *J. Phys. Chem. Lett.* **2018**, *9*, 874–880.
[47] O. N. Antzutkin, S. C. Shekar, M. H. Levitt, *J. Magn. Reson. Ser. A* **1995**, *115*, 7–19.

[48] M. Baias, J.-N. Dumez, P. H. Svensson, S. Schantz, G. M. Day, L. Emsley, *J. Am. Chem. Soc.* **2013**, *135*, 17501–17507.
[49] P. Hodgkinson, *Prog. Nucl. Magn. Reson. Spectrosc.* **2020**, *118–119*, 10–53.
[50] D. H. Brouwer, *J. Am. Chem. Soc.* **2008**, *130*, 6306–6307.
[51] A. Kumar, B. J. Walder, A. Kunhi Mohamed, A. Hofstetter, B. Srinivasan, A. J. Rossini, K. Scrivener, L. Emsley, P. Bowen, *J. Phys. Chem. C* **2017**, *121*, 17188–17196.
[52] M. A. Hope, T. Nakamura, P. Ahlawat, A. Mishra, M. Cordova, F. Jahanbakhshi, M. Mladenović, R. Runjhun, L. Merten, A. Hinderhofer, B. I. Carlsen, D. J. Kubicki, R. Gershoni-Poranne, T. Schneeberger, L. C. Carbone, Y. Liu, S. M. Zakeeruddin, J. Lewinski, A. Hagfeldt, F. Schreiber, U. Rothlisberger, M. Grätzel, J. V. Milić, L. Emsley, *J. Am. Chem. Soc.* **2021**, *143*, 1529–1538.
[53] E. van Lenthe, E. J. Baerends, J. G. Snijders, *J. Chem. Phys.* **1993**, *99*, 4597–4610.
[54] E. van Lenthe, E. J. Baerends, J. G. Snijders, *J. Chem. Phys.* **1994**, *101*, 9783–9792.
[55] F. Alkan, C. Dybowski, *Phys. Chem. Chem. Phys.* **2015**, *17*, 25014–25026.
[56] A. J. Rossini, A. W. Macgregor, A. S. Smith, G. Schatte, R. W. Schurko, G. G. Briand, *Dalton Trans.* **2013**, *42*, 9533–9546.
[57] D. Srivastava, M. Giammar, M. Venetos, A. McCarthy, G. Philip, *Zenodo*: 10.5281/zenodo.6892947, **2022**.
[58] Y.-S. Kye, S. Connolly, B. Herreros, G. S. Harbison, *Main Group Met. Chem.* **1999**, *22*, 373–383.
[59] K. Shibuya, M. Koshimizu, F. Nishikido, H. Saito, S. Kishimoto, *Acta Crystallogr. Sect. E* **2009**, *65*, m1323–m1324.
[60] M. D. Smith, A. Jaffe, E. R. Dohner, A. M. Lindenberg, H. I. Karunadasa, *Chem. Sci.* **2017**, *8*, 4497–4504.

Manuscript received: October 4, 2023
Accepted manuscript online: February 2, 2024
Version of record online: February 19, 2024